Modeling acoustic space-coiled metacrystals

Joar Zhou Hagström, Kim Pham, Agnés Maurel

MODELLING ACOUSTIC SPACE-COILED METACRYSTALS*

JOAR ZHOU HAGSTRÖM †, KIM PHAM †, AND AGNÈS MAUREL ‡

Abstract. We present an effective model of "space-coiled metacrystals" composed of a periodic array of sound rigid blocks into which long slots have been coiled up. The periodic cell of the block contains a coiled slot whose straight parts are at wavelength scale, which enables the appearance of Bragg resonances. These resonances, which prevent high transmission, compete with the Fabry-Pérot resonances of the entire slot, which foster perfect transmission. This results in complex scattering properties driven by the characteristics of the turning regions that act as atoms in a one-dimensional coiled crystal. Using appropriate scaling and combining two-scale homogenization with matched asymptotic techniques, the modelling of such metacrystals is proposed. The resulting model is validated through a comparison with full-wave numerics in both harmonic and transient regimes.

Key words. Space-coiling, resonant metasurface, crystal, two-scale homogenization, asymptotic analysis

AMS subject classifications. 34E13, 35B27, 35L05, 76B15

1. Introduction. Many devices used to control the propagation of acoustic waves are based on arrangements of guiding slots. The simplest example is that of a sound-rigid wall pierced by a regular array of straight slots whose periodicity is less than the wavelength. When the wall has a thickness comparable to the wavelength, Fabry-Pérot type resonances appear, which have been exploited for practical applications [12, 2]. About ten years ago, the idea emerged that it would be possible to use devices with sub-wavelength thicknesses, called "metasurfaces", capable of interacting strongly with waves [20]. With this in mind, Liang and Li [11] proposed to promote the straight slot array into the family of metasurfaces by rolling up the slots in the unit cell with the intuitive idea that the straight slots and their rolled-up version behave in the same way. Based on this concept of spaced-coil structures, applications have been proposed for the acoustic lensing [8, 16, 17], unidirectional transmission [7, 16, 9] and negative refraction [19, 10]. From a theoretical point of view, a heuristic model was initially proposed in [9, 1], which is essentially based (but not explicitly stated) on the homogenisation of a straight slit grating whose length is that of the uncoiled path. Such approaches are justified for these structures since the dimensions of the unit cell are subwavelength, but this implies that the straight parts of the labyrinth between the turning regions are also subwavelength [21]. As a result, the scattering turning regions have only a weak effect on wave propagation and the labyrinthine structure behaves as a homogeneous anisotropic block producing perfect transmissions at the Fabry-Pérot resonances at low frequencies.

In the present study, we consider labyrinths whose longest straight parts (of length ℓ, see figure 1(a)) are of wavelength size. This way, the turning regions have strong scattering effects that make possible the appearance of Bragg band-gaps, as they behave like the atoms of a one-dimensional coiled crystal. Besides, we keep the peri-

*Submitted to the editors DATE.

Funding: K.P. and J.Z.H. acknowledge support from the Agence de l'Innovation de Défense (AID) from the Direction Générale de l'Armement (DGA), under grant no. 2019 65 0070 and 2019 65 0042, and the Agence Nationale de la Recherche under grant ANR-19-CE08-0006. A.M. acknowledges the support of the Agence Nationale de la Recherche (ANR) under grant 243560 CoProMM.

†IMSIA, CNRS, EDF, CEA, ENSTA Paris, Institut Polytechnique de Paris, 828 Bd des Maréchaux, 91732 Palaiseau, France, (joar.zhou-hagstrom@ensta-paris.fr, kim.pham@ensta-paris.fr)

‡ESPCI Paris, PSL University, CNRS, Institut Langevin, France, (agnes.maurel@espci.fr)

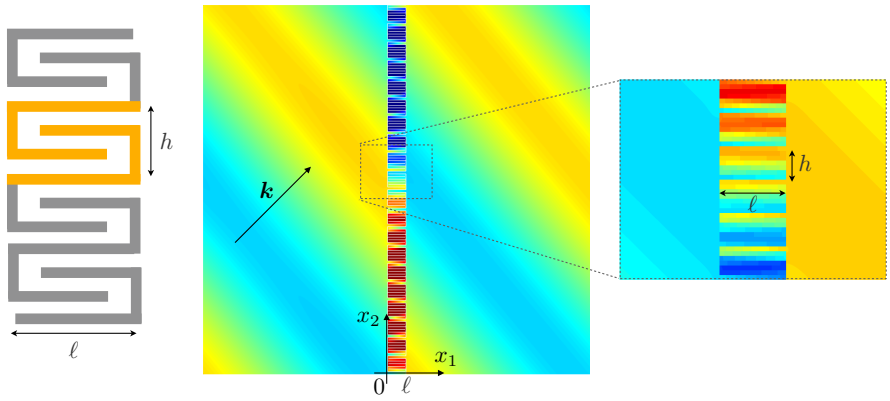

FIG. 1. *(a) Geometry of the space-coiled metacrystal; the unit cell (in orange) contains a coiled slot whose straight parts, of length ℓ, are of wavelength size while the periodicity h is subwavelength. (b) Scattering of an incident wave with wavevector $\boldsymbol{k}$; the reported fields have been calculated numerically for an incident plane wave at incidence 45° ($k\ell = 0.41$, $\ell = 2h$ with zero wall thicknesses).*

odicity h of the structure on a subwavelength scale so that both the Bragg resonances and the Fabry-Pérot resonances of the entire (uncoiled) slot occur in a low frequency regime, *i.e.*, in a regime where the grating supports a single diffraction order. It results in a complex scattering due to the competition between the two types of resonances, the Fabry-Pérot resonances fostering high transmission and the Bragg resonances preventing it. In what follows, we build an effective model that captures these scattering properties. To do so, we combine model reduction in straight regions to capture propagation, two-scale homogenization to deal with periodicity, and suitable asymptotic techniques to deal with the evanescent field triggered in the turning regions and at the labyrinth extremities. The paper is organized as follows. In §2, we present the effective model whose derivation is detailed in §3. The derivation is performed in the time domain, which allows us to discuss the energy properties of the effective model; this is done in §4. The validation of the model is presented in §5 by comparisons with direct numerical calculations in the harmonic and transient domains.

2. Main results.

2.1. The actual problem. We consider the scattering of acoustic waves by a metacrystal as shown in figure 1. It is made of a periodic arrangement of unit cells along the vertical, x_2, direction with subwavelength periodicity h and horizontal thickness ℓ (along x_1). Each cell contains a coiled slot resulting in N horizontal slots connected between them through turning regions. Note that for a transmissive structure, N is odd ($N = 1$ corresponds to a straight, uncoiled, slot and we show the case $N = 3$ in figure 1). In the air, the acoustic pressure p and velocity $\boldsymbol{u}$ satisfy the linearized Euler equations

$$\frac{\partial \boldsymbol{u}}{\partial t} = -\frac{1}{\rho_{\mathrm{a}}}\boldsymbol{\nabla} p, \quad \chi_{\mathrm{a}}\frac{\partial p}{\partial t} + \mathrm{div}\boldsymbol{u} = 0, \quad \boldsymbol{u}\cdot\boldsymbol{n}_{|\Gamma} = 0, \tag{2.1}$$

where $(\rho_{\mathrm{a}}, \chi_{\mathrm{a}})$ are the mass density and the compressibility of the air (and t is the time). The problem is complemented by Neumann boundary conditions on the pressure (vanishing normal velocity) applying on the boundaries Γ of the sound-rigid walls.

2.2. The effective problem. In the effective model, whose derivation is detailed in the forthcoming §3, we distinguish two regions, as sketched in figure 2. In the regions surrounding the metacrystal, for $x_1 \notin (0,\ell)$, the linearized Euler equations apply, namely

$$\frac{\partial \boldsymbol{u}}{\partial t} = -\frac{1}{\rho_{\mathrm{a}}}\boldsymbol{\nabla} p, \qquad \chi_{\mathrm{a}}\frac{\partial p}{\partial t} + \mathrm{div}\boldsymbol{u} = 0, \qquad \text{for } x_1 \notin (0,\ell), \tag{2.2}$$

with p and $\boldsymbol{u}$ depending of $\boldsymbol{x}$ and t as in the actual problem.

In the metacrystalline region $x_1 \in (0,\ell)$, we denote (P,U) the acoustic pressure and velocity, respectively. This region is described in terms of a strongly anisotropic effective medium, the spatial variable x_1 being replaced by the curvilinear abscissa s, $s \in (0, L_t)$ with $L_t = N\ell$ the total length of the coiled slot. In each straight part of the slot, for $s \in (s_n^+, s_{n+1}^-)$, $n \in \{0,\dots,N-1\}$, (blue segments associated with specific s-orientation in figure 2), (P,U) satisfy the one-dimensional propagation equations

$$\frac{\partial U}{\partial t} = -\frac{\delta}{\rho_{\mathrm{a}}}\frac{\partial P}{\partial s}, \qquad \chi_{\mathrm{a}}\delta\frac{\partial P}{\partial t} + \frac{\partial U}{\partial s} = 0, \quad \text{for } s \in (s_n^+, s_{n+1}^-), \tag{2.3}$$

where

$$s_0^+ = 0, \quad s_N^- = N\ell, \quad \text{and } s_n^\pm = n\ell \pm e, n \in \{0,\dots,N-1\}, \tag{2.4}$$

with $e = (\eta+\gamma)h$ the width of the turning region (δ, η and γ are non-dimensional geometrical parameters defined in figure 3). Note that the fields (P,U) depend on s which allows us to describe the propagation within a single cell but they also depend on x_2 which allows us to describe the field variations from one cell to the others (and they depend on time t). Next, the effect of a turning region connecting two consecutive slots (sketched in red in figure 2) is encapsulated in jump conditions of the form

$$\begin{cases} [\![P]\!]_n = -\rho_{\mathrm{a}} h\mathcal{D}\dfrac{\partial \langle U\rangle_n}{\partial t} - h(\delta+\xi)\dfrac{\partial \langle P\rangle_n}{\partial x_2}, \\ [\![U]\!]_n = -\chi_{\mathrm{a}} h(2\delta+\xi)\eta\dfrac{\partial \langle P\rangle_n}{\partial t} - h(\delta+\xi)\dfrac{\partial \langle U\rangle_n}{\partial x_2}, \end{cases} \tag{2.5}$$

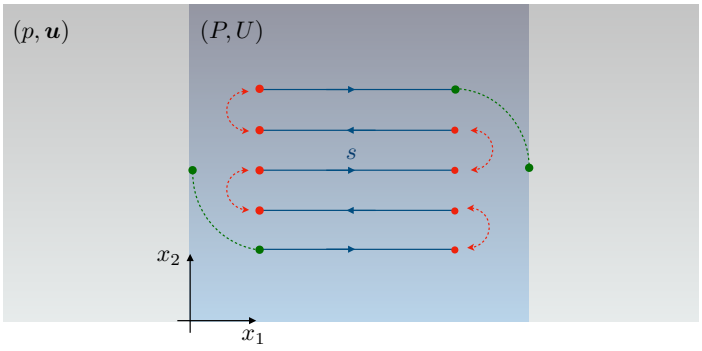

FIG. 2. *The effective problem where the unit cell of the metacrystal has been replaced by a homogenized anisotropic region with one-dimensional propagation. It is set on a curvilinear coordinate s that follows the coiled path (blue lines). Jump conditions account for boundary layer effects in the turning regions (red dotted lines) and at the extremities of the coiled slot connected to the surrounding air (green dotted lines). The actual rigid, pierced, block is shown in light grey to assist in the understanding.*

for $n \in \{1, \dots, N-1\}$ (ξ is a non-dimensional geometrical parameter defined in figure 3), and where the jump and the average of the field $F = (P, U)$ are defined by

$$[\![F]\!]_n = F(s_n^+, x_2, t) - F(s_n^-, x_2, t), \quad \langle F \rangle_n = \frac{1}{2}\left(F(s_n^+, x_2, t) + F(s_n^-, x_2, t)\right).$$

Eventually at the extremities $s = s_0^+$ and $s = s_N^-$ of the coiled slot, which communicate with the surrounding air at $x_1 = 0$ and $x_1 = \ell$ (these regions are sketched in green in figure 2), jump conditions of a different type apply, of the form

$$n \in \{0, N\}, \quad \begin{cases} [\![P]\!]_n = -\rho_a h \mathcal{B} \dfrac{\partial \langle U \rangle_n}{\partial t}, \\ [\![U]\!]_n = -h\mathcal{C} \dfrac{\partial W_n}{\partial x_2}, \quad \text{where} \quad \dfrac{\partial W_n}{\partial t} = -\dfrac{1}{\rho_a} \dfrac{\partial \langle P \rangle_n}{\partial x_2}, \end{cases} \tag{2.6}$$

where we have defined, for $f = (p, u_1)$ and $F = (P, U)$, the jumps

$$\begin{cases} [\![F]\!]_0 = F(s_0^+, x_2, t) - f(0^-, x_2, t), \quad \langle F \rangle_0 = \dfrac{1}{2}\left(F(s_0^+, x_2, t) + f(0^-, x_2, t)\right), \\ [\![F]\!]_N = f(\ell^+, x_2, t) - F(s_N^-, x_2, t), \quad \langle F \rangle_N = \dfrac{1}{2}\left(f(\ell^+, x_2, t) + F(s_N^-, x_2, t)\right). \end{cases}$$

The effective model involves, in addition to geometrical parameters, three effective parameters $(\mathcal{B}, \mathcal{C}, \mathcal{D})$ which are boundary layer coefficients given by elementary static problems that will appear in the asymptotic analysis.

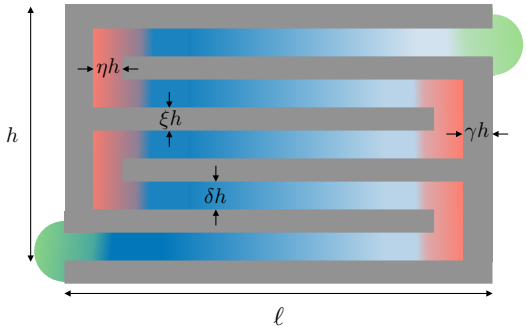

FIG. 3. *Decomposition of the unit cell into sub-regions requiring appropriate asymptotic analysis. In the straight parts of the coiled slot (blue area) the propagation is accounted for; in the turning regions connecting two of these straight slots (red area) and in the regions connecting the extremities of the coiled slot to the surrounding air (green area), matched asymptotic methods are used to capture the effect of the boundary layers.*

We notice that the model results from an analysis conducted at order 1 with respect to the small parameter $kh \ll 1$ which is a measure of the subwavelength regime. We will see in the forthcoming section that the model at order 0 (limit problem) is trivial because it corresponds to an uncoiled slot. This means that, in the $x_1 \in (0, \ell)$ crystalline region, (2.3) applies to the whole uncoiled slot, i.e., $s \in (0, N\ell)$, since the jump conditions in (2.5) reduce to continuity conditions $[\![P]\!]_n = [\![U]\!]_n = 0$. The same is true at the ends $s = 0$ and $s = N\ell$ in (2.6) (without effect of evanescent fields triggered at the junction of a slot with the surrounding regions). By neglecting the evanescent fields at the extremities of the slot, the model at order 0 gives a rough

estimate of the Fabry-Pérot resonances. This is true for straight slots and the (mild) gain obtained with the model at order 1 has been discussed in [14]. In contrast, by neglecting the effects of evanescent fields in the turning regions, the model at order 0 completely misses the Bragg resonances. We will see in §5 that this results in a serious lack of accuracy.

3. Derivation of the effective model. We derive in this section the effective model based on asymptotic analysis valid in the subwavelength regime which means that the typical wavelength is much smaller than the unit cell length h. As we are working in the time domain, the subwavelength regime implicitly assumes that the spectral content of the sources, once they will be defined, is limited by a maximum angular frequency ω satisfying

$$\varepsilon = kh \ll 1, \qquad k = \omega/c,$$

with $c = 1/\sqrt{\rho_{\rm a}\chi_{\rm a}}$ the speed of sound. We also consider

$$k\ell = O(1), \qquad \eta, \xi, \delta, \gamma = O(1),$$

hence $N = O(1)$ (see figure 3). In the following, we shall use non-dimensional forms of the linearized Euler equations (2.1), with

$$p \to \chi_{\rm a} p, \quad \boldsymbol{u} \to \boldsymbol{u}/c, \quad t \to \omega t, \quad \boldsymbol{x} \to \omega \boldsymbol{x}/c, \tag{3.1}$$

resulting in

$$\frac{\partial \boldsymbol{u}}{\partial t} = -\boldsymbol{\nabla} p, \quad \frac{\partial p}{\partial t} + \mathrm{div}\boldsymbol{u} = 0, \quad \boldsymbol{u}\cdot\boldsymbol{n}_{|\Gamma} = 0. \tag{3.2}$$

In the asymptotic procedure, we shall consider sub-regions where appropriate analysis will be achieved. Specifically, as sketched in figure 3 (the figure uses the same color code as in figure 2), we shall distinguish the straight parts of the coiled slot (blue area) where one-dimensional wave propagation takes place resulting in (2.3), the turning regions connecting two straight slots (red area) and eventually the regions connecting the coiled slot to the surrounding air (green area). These two families of intermediate regions involve evanescent fields whose signatures in the effective model are the jump conditions announced in (2.5) and (2.6).

3.1. Effective propagation in the straight parts of the coiled slot.

3.1.1. Setting of the asymptotic procedure. In the straight slots far from the turning regions, the medium is structured along x_2 only. Hence, we assume the following expansions

$$p^\varepsilon = \sum_{i\geqslant 0} \varepsilon^i p^i(\boldsymbol{x}, y_2, t)\ , \qquad \boldsymbol{u}^\varepsilon = \sum_{i\geqslant 0} \varepsilon^i \boldsymbol{u}^i(\boldsymbol{x}, y_2, t) \quad \text{with} \quad \boldsymbol{u}^i = u^i \boldsymbol{e}_1 + v^i \boldsymbol{e}_2, \tag{3.3}$$

where $(\boldsymbol{e}_1, \boldsymbol{e}_2)$ are the unit vectors along x_1 and x_2. The variable $y_2 = x_2/\varepsilon \in (0,1)$ is a fast variable describing the vertical position towards the N slots. We denote $Y_{(n)}$ the region of the n-th slot within the unit cell $y_2 \in (0,1)$, specifically

$$Y_{(n)} = (y_{(n)} - \delta/2, y_{(n)} + \delta/2), \quad y_{(n)} = (n-1)(\delta+\xi) + \delta/2, \tag{3.4}$$

see figure 4. For the n-th slot and at any order i, we define the average pressure field $p^i_{(n)}$ and the flow rate $u^i_{(n)}$ as

$$p^i_{(n)}(\boldsymbol{x},t) = \frac{1}{\delta}\int_{Y_{(n)}} p^i(\boldsymbol{x},y_2,t)\,\mathrm{d}y_2, \quad u^i_{(n)}(\boldsymbol{x},t) = \int_{Y_{(n)}} u^i(\boldsymbol{x},y_2,t)\,\mathrm{d}y_2, \tag{3.5}$$

which are the effective, macroscopic, fields we are interested in. The Neumann condi-

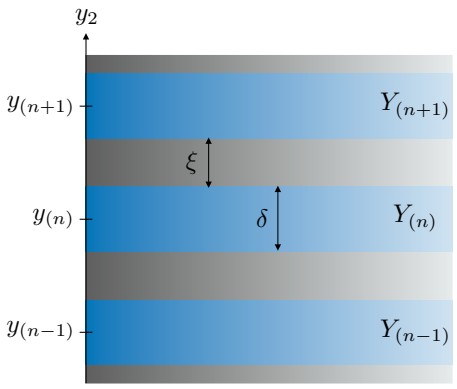

FIG. 4. *The one-dimensional representative cell defined by $y_2 \in (0,1)$ inside the coiled region far from the extremities. It is made of N segments of thickness δ (blue region) separated by walls of thickness ξ (grey region).*

tion on the horizontal rigid walls, separating each slot from the other, holds at each order of the expansion and reads

$$v^i(\boldsymbol{x}, y_{(n)} \pm \delta/2, t) = 0. \tag{3.6}$$

Due to the two-scale expansions in (3.3), the divergence operator and the gradient operator now read

$$\mathrm{div}\boldsymbol{f} = \mathrm{div}_{\boldsymbol{x}}\boldsymbol{f} + \frac{1}{\varepsilon}\frac{\partial \boldsymbol{f}}{\partial y_2}\cdot\boldsymbol{e}_2, \qquad \boldsymbol{\nabla} f = \boldsymbol{\nabla}_{\boldsymbol{x}} f + \frac{1}{\varepsilon}\frac{\partial f}{\partial y_2}\boldsymbol{e}_2, \tag{3.7}$$

for any vectorial function $\boldsymbol{f}(\boldsymbol{x},y_2,t)$ and for any scalar function $f(\boldsymbol{x},y_2,t)$. Accordingly, applying the differential operators (3.7) to (3.2) along with (3.3) and identifying the terms with same powers in ε, we obtain

$$\begin{cases} \dfrac{\partial v^0}{\partial y_2} = 0, \quad \dfrac{\partial p^i}{\partial t} + \mathrm{div}_{\boldsymbol{x}}\boldsymbol{u}^i + \dfrac{\partial v^{i+1}}{\partial y_2} = 0 \quad \text{for } i \geq 0, \\ \dfrac{\partial p^0}{\partial y_2} = 0, \quad \dfrac{\partial \boldsymbol{u}^i}{\partial t} = -\boldsymbol{\nabla}_{\boldsymbol{x}} p^i - \dfrac{\partial p^{i+1}}{\partial y_2}\boldsymbol{e}_2 \quad \text{for } i \geq 0. \end{cases} \tag{3.8}$$

3.1.2. The order 0 in the slots. We deduce from the leading order in (3.8) that p^0 and v^0 take constant values in each slot (yet possible different values due to the rigid walls between the slots). Using the definition (3.5) of the average, we get

$$p^0(\boldsymbol{x}, y_2 \in Y_{(n)}, t) = p^0_{(n)}(\boldsymbol{x},t). \tag{3.9}$$

and from the Neumann boundary conditions (3.6), we have

$$v^0(\boldsymbol{x}, y_2 \in Y_{(n)}, t) = 0. \tag{3.10}$$

At the next order in (3.8), we obtain that $\frac{\partial u^0}{\partial t} = -\frac{\partial p^0}{\partial x_1}$ with p^0 piecewise constant. We deduce using (3.5) that

$$\boldsymbol{u}^0(\boldsymbol{x}, y_2 \in Y_{(n)}, t) = \frac{1}{\delta} u^0_{(n)}(\boldsymbol{x}, t)\boldsymbol{e}_1.$$

Next, integrating the mass balance in (3.8) at order $i = 0$ over $Y_{(n)}$ and using (3.5) as well as Neumann boundary conditions (3.6) to get rid of the contribution of v^1 at the walls, we also obtain

$$\frac{\partial u^0_{(n)}}{\partial t} + \delta \frac{\partial p^0_{(n)}}{\partial x_1} = 0, \qquad \frac{\partial u^0_{(n)}}{\partial x_1} + \delta \frac{\partial p^0_{(n)}}{\partial t} = 0, \tag{3.11}$$

which describes the expected one-dimensional propagation in the n-th slot.

3.1.3. The order 1 in the slots. From the balance of mass given by (3.8) (with $i = 0$) and equations (3.9) and (3.11) derived at the dominant order, we get that $\frac{\partial p^0}{\partial t} + \mathrm{div}_{\boldsymbol{x}} \boldsymbol{u}^0 = 0$, hence we have $\partial_{y_2} v^1 = 0$ and v^1 is piecewise constant. By taking into account the Neumann boundary conditions (3.6) at order 1, we deduce that $v^1 = 0$ in all the slots. From the balance of momentum in (3.8) along $\boldsymbol{e}_2$ at order 0 and (3.10), we have $0 = -\frac{\partial p^1}{\partial y_2} - \frac{\partial p^0}{\partial x_2}$, which after integration gives

$$p^1 = (y_{(n)} - y_2)\frac{\partial p^0_{(n)}}{\partial x_2} + p^1_{(n)}, \tag{3.12}$$

with $\int_{Y_{(n)}} (y_{(n)} - y_2)\, \mathrm{d}y_2 = 0$. Integrating the mass balance (3.8) for $i = 1$ and using the Neumann boundary conditions (3.6), we get the one-dimensional wave equation at the first order in the n-th slot

$$\frac{\partial u^1_{(n)}}{\partial t} + \delta \frac{\partial p^1_{(n)}}{\partial x_1} = 0, \qquad \frac{\partial u^1_{(n)}}{\partial x_1} + \delta \frac{\partial p^1_{(n)}}{\partial t} = 0, \tag{3.13}$$

which is the same as the one obtained at order 0.

3.2. Solutions in the air far from the material. Since the surrounding air for $x_1 \notin (0, \ell)$ is a homogeneous medium, the asymptotic expansion is straightforward and does not involve two scales expansion. Specifically, we have

$$p^\varepsilon = \sum_{i \geqslant 0} \varepsilon^i p^i(\boldsymbol{x}, t)\,, \qquad \boldsymbol{u}^\varepsilon = \sum_{i \geqslant 0} \varepsilon^i \boldsymbol{u}^i(\boldsymbol{x}, t), \tag{3.14}$$

which after injection in (3.2) results at each order in

$$\forall i \geq 0, \quad \frac{\partial p^i}{\partial t} + \mathrm{div}_{\boldsymbol{x}} \boldsymbol{u}^i = 0\,, \qquad \frac{\partial \boldsymbol{u}^i}{\partial t} = -\boldsymbol{\nabla}_{\boldsymbol{x}} p^i. \tag{3.15}$$

3.3. Analysis at the junctions at the entry/exit of the slot. We shall now derive the effective jump conditions applying between the extremities of the coiled slot and the surrounding air. The analysis is presented at the extremity $x_1 = 0$ as the jump conditions at $x_1 = \ell$ can be deduced by mirroring the analysis.

3.3.1. Setting of the asymptotic procedure. It consists in matching the *outer* expansions (3.3) and (3.14) through an intermediate inner region governed by boundary layer effect. To do that, we introduce the representative unit cell $\mathcal{Y}$, obtained by rescaling spatially the extremity of the slot near $x_1 = 0$ owing to the variable $\boldsymbol{y} = \boldsymbol{x}/\varepsilon$, see figure 5. This cell is the union $\mathcal{Y} = \mathcal{Y}^+ \cup \mathcal{Y}^-$ of the semi-infinite

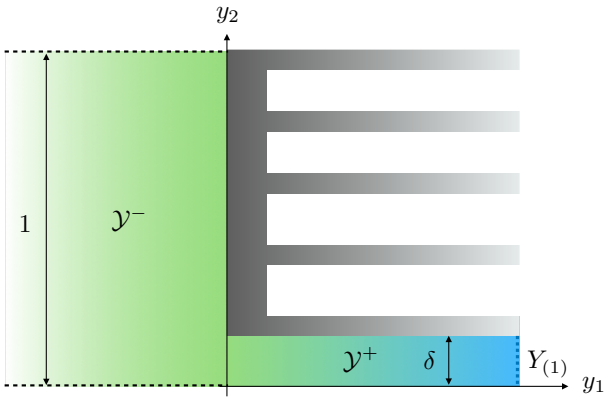

FIG. 5. *The representative unit cell $\mathcal{Y} = \mathcal{Y}^+ \cup \mathcal{Y}^-$ near one extremity of the slot at $x_1 = 0$ connects the surrounding air (green region) to the interior of the slot (blue region).*

region $\mathcal{Y}^-$ in the surrounding fluid and of the semi-infinite region $\mathcal{Y}^+$ in the first straight slot, specifically

$$\mathcal{Y}^- = (-\infty, 0) \times (0, 1), \qquad \mathcal{Y}^+ = (0, \infty) \times Y_{(1)}.$$

In this inner region, we use the following expansion of the fields

$$p^\varepsilon = \sum_{i \geqslant 0} \varepsilon^i \mathsf{p}^i(x_2, \boldsymbol{y}, t)\,, \qquad \boldsymbol{u}^\varepsilon = \sum_{i \geqslant 0} \varepsilon^i \mathbf{u}^i(x_2, \boldsymbol{y}, t), \quad \mathbf{u} = (\mathsf{u}, \mathsf{v}), \tag{3.16}$$

where $(\mathsf{p}^i, \mathbf{u}^i)$ are assumed to be periodic with respect to y_2 in $\mathcal{Y}^-$ and $\mathbf{u}^i \cdot \boldsymbol{n} = 0$ on the boundaries Γ of the rigid walls. As in the previous section, the divergence operator and the gradient operator are affected by the two-scale expansion, which in this case read

$$\mathrm{div}\boldsymbol{f} = \frac{\partial \boldsymbol{f}}{\partial x_2} \cdot \boldsymbol{e}_2 + \frac{1}{\varepsilon} \mathrm{div}_{\boldsymbol{y}} \boldsymbol{f}, \qquad \boldsymbol{\nabla} f = \frac{\partial f}{\partial x_2} \cdot \boldsymbol{e}_2 + \frac{1}{\varepsilon} \boldsymbol{\nabla}_{\boldsymbol{y}} f,$$

for any vectorial function $\boldsymbol{f}(x_2, \boldsymbol{y})$ and for any scalar function $f(x_2, \boldsymbol{y})$. Injecting the expansions (3.16) in (3.2), we get at the leading orders

$$\begin{cases} \mathrm{div}_y \mathbf{u}^0 = 0, \quad \mathrm{div}_y \mathbf{u}^1 + \partial_{x_2} \mathsf{v}^0 + \dfrac{\partial \mathsf{p}^0}{\partial t} = 0, \\ 0 = \boldsymbol{\nabla}_y \mathsf{p}^0, \quad \dfrac{\partial \mathbf{u}^0}{\partial t} = -\dfrac{\partial \mathsf{p}^0}{\partial x_2} \boldsymbol{e}_2 - \boldsymbol{\nabla}_y \mathsf{p}^1, \\ \mathbf{u}^0 \cdot \boldsymbol{n}_{|\Gamma} = \mathbf{u}^1 \cdot \boldsymbol{n}_{|\Gamma} = 0. \end{cases} \tag{3.17}$$

The matching conditions are obtained by pairing the outer expansions (3.3) and (3.14) valid far from the entry at $y_1 = 0$ with the inner expansions (3.16) valid in the vicinity

of the entry. For the pressure expansions in (3.14) and (3.16), the matching reads

$$\mathsf{p}^0(x_2,\boldsymbol{y},t)+\varepsilon\mathsf{p}^1(x_2,\boldsymbol{y},t)+\cdots\sim p^0(\boldsymbol{x},t)+\varepsilon p^1(\boldsymbol{x},t)+\cdots,$$

as $y_1\to-\infty$ and $x_1\to 0^-$. By recalling that $x_1=\varepsilon y_1$ and by using a Taylor expansion of the outer expansion with respect to ε, we get at the dominant order and at the first order in the fluid

$$p^0(0^-,x_2,t)=\lim_{y_1\to-\infty}\mathsf{p}^0(x_2,\boldsymbol{y},t), \tag{3.18}$$

$$p^1(0^-,x_2,t)=\lim_{y_1\to-\infty}\left(\mathsf{p}^1(x_2,\boldsymbol{y},t)-y_1\frac{\partial p^0}{\partial x_1}(0^-,x_2,t)\right). \tag{3.19}$$

Doing the same for the expansions in (3.3) and (3.16) results in

$$\mathsf{p}^0(x_2,\boldsymbol{y},t)+\varepsilon\mathsf{p}^1(x_2,\boldsymbol{y},t)+\cdots\sim p^0(\boldsymbol{x},y_2,t)+\varepsilon p^1(\boldsymbol{x},y_2,t)+\cdots,$$

as $y_1\to+\infty$ (with $y_2\in Y_{(1)}$) and $x_1\to 0^+$, hence for $y_2\in Y_{(1)}$, we get

$$p^0(0^+,x_2,y_2,t)=\lim_{y_1\to+\infty}\mathsf{p}^0(x_2,\boldsymbol{y},t), \tag{3.20}$$

$$p^1(0^+,x_2,y_2,t)=\lim_{y_1\to+\infty}\left(\mathsf{p}^1(x_2,\boldsymbol{y},t)-y_1\frac{\partial p^0}{\partial x_1}(0^+,x_2,y_2,t)\right). \tag{3.21}$$

The exact same matching conditions as (3.18) and (3.20) are obtained for the velocity field by replacing formally p by $\mathbf{u}$ and p by $\boldsymbol{u}$.

3.3.2. The continuity conditions at order 0. From (3.17), we deduce that p^0 is independent of $\boldsymbol{y}$ and we obtain from the matching conditions (3.18) and (3.20) that

$$p^0_{(1)}(0^+,x_2,t)=\mathsf{p}^0(x_2,\boldsymbol{y},t)=p^0(0^-,x_2,t), \tag{3.22}$$

since $p^0=p^0_{(1)}$ for $y_2\in Y_{(1)}$ from (3.9). Next, by integrating the free divergence equation in (3.17) set on $\mathbf{u}^0$ over the subset domain $\mathcal{Y}^*\subset\mathcal{Y}$, truncated at $y_1=\pm y_1^*$ with $y_1^*\gg 1$, and using the Neumann boundary conditions on the rigid walls and the periodic boundary condition in $\mathcal{Y}^*\cap\mathcal{Y}^-$, we obtain

$$\int_{Y_{(1)}}\mathsf{u}^0(x_2,y_1^*,y_2,t)\,\mathrm{d}y_2-\int_{Y}\mathsf{u}^0(x_2,-y_1^*,y_2,t)\,\mathrm{d}y_2=0.$$

Passing to the limit as $y_1^*\to+\infty$ and using the matching conditions (3.18) and (3.20) written on the velocity, we obtain

$$u^0_{(1)}(0^+,x_2,t)=u^0(0^-,x_2,t). \tag{3.23}$$

Therefore, there is no boundary layer correction at the, dominant, order 0 meaning that the usual continuity conditions on pressure and flow rate apply. Conducting the same analysis at the extremity $x_1=\ell$ of the slot, we get the same continuity conditions, namely

$$p^0_{(N)}(\ell^-,x_2,t)=p^0(\ell^+,x_2,t),\quad u^0_{(N)}(\ell^-,x_2,t)=u^0(\ell^+,x_2,t).$$

3.3.3. The jump conditions at order 1.

Jump condition on the pressure. From (3.17), the problem set on $\mathcal{Y}$ for the couple $(\mathsf{p}^1, \mathbf{u}^0)$ is given by

$$\begin{cases} \dfrac{\partial \mathbf{u}^0}{\partial t} = -\dfrac{\partial p^0}{\partial x_2}\Big|_{0^-} \boldsymbol{e}_2 - \boldsymbol{\nabla}_y \mathsf{p}^1 \ , \quad \mathrm{div}_y \mathbf{u}^0 = 0 \ , \quad \mathbf{u}^0 \cdot \boldsymbol{n}_{|\Gamma} = 0 \ , \\ \lim\limits_{y_1 \to -\infty} \dfrac{\partial \mathbf{u}^0}{\partial t} = \dfrac{\partial u^0}{\partial t}\Big|_{0^-} \boldsymbol{e}_1 - \dfrac{\partial p^0}{\partial x_2}\Big|_{0^-} \boldsymbol{e}_2, \\ \lim\limits_{y_1 \to +\infty} \dfrac{\partial \mathbf{u}^0}{\partial t} = \dfrac{1}{\delta} \dfrac{\partial u^0}{\partial t}\Big|_{0^-} \boldsymbol{e}_1, \end{cases} \tag{3.24}$$

with $\frac{\partial p^0}{\partial x_2}|_{0^-} = \frac{\partial p^0}{\partial x_2}(0^-, x_2, t)$ and $\frac{\partial u^0}{\partial t}|_{0^-} = \frac{\partial u^0}{\partial t}(0^-, x_2, t)$. In (3.24), we have used the continuities of the pressure and of the flow rate given by (3.22) and (3.23), along with (3.9) (for $n = 1$). By linearity, the solution of (3.24) can be decomposed as a linear combination of the macroscopic fields $\frac{\partial p^0}{\partial x_2}|_{0^-}$ and $\frac{\partial u^0}{\partial t}|_{0^-}$ which do not depend on $\boldsymbol{y}$. Specifically, we have

$$\mathsf{p}^1(x_2, \boldsymbol{y}, t) = \frac{\partial p^0}{\partial x_2}\Big|_{0^-} Q_2(\boldsymbol{y}) - \frac{\partial u^0}{\partial t}\Big|_{0^-} Q_1(\boldsymbol{y}) + Q_*(x_2, t), \tag{3.25}$$

where the functions (Q_1, Q_2) satisfy the so-called elementary problems given by ($i = 1, 2$)

$$i \in \{1, 2\}, \begin{cases} \mathrm{div}_y(\boldsymbol{\nabla}_y Q_i + \delta_{i2}\boldsymbol{e}_2) = 0 \ \text{ in } \mathcal{Y}, \quad (\boldsymbol{\nabla}_y Q_i + \delta_{i2}\boldsymbol{e}_2) \cdot \boldsymbol{n}_{|\Gamma} = 0, \\ (Q_i, \boldsymbol{\nabla} Q_i) \quad y_2 - \text{ periodic for } \quad y_1 < 0, \\ \lim\limits_{y_1 \to -\infty} \boldsymbol{\nabla}_y Q_i = \delta_{i1}\boldsymbol{e}_1, \quad \lim\limits_{y_1 \to +\infty} \boldsymbol{\nabla}_y Q_i = \delta_{i1}\boldsymbol{e}_1/\delta - \delta_{i2}\boldsymbol{e}_2, \end{cases} \tag{3.26}$$

with $\delta_{ij} = 0$ if $i \neq j$ and $\delta_{ij} = 1$ otherwise. The behavior of (Q_1, Q_2) at infinity reads

(3.27)

	$\lim\limits_{y_1 \to -\infty}$	$\lim\limits_{y_1 \to +\infty}$
Q_1	y_1	$\dfrac{y_1}{\delta} + \mathcal{B}$
Q_2	0	$y_{(1)} - y_2$

with $y_{(1)} = \delta/2$ from (3.4). Note that the problem on Q_1 corresponds to a classical potential flow problem and in this context, $\mathcal{B}$ is called *blockage* coefficient [15]. For Q_1 which corresponds to the problem of a perfect fluid flowing in a rigid duct whose height changes from 1 for $y_1 < 0$ to δ for $y_1 > 0$, $\mathcal{B}$ has been determined by [18] (Eq. (2.12)), namely

$$\mathcal{B} = \frac{1}{2\pi} \left[\frac{1 + \delta^2}{\delta} \log \frac{1 + \delta}{1 - \delta} - 2 \log \frac{4\delta}{1 - \delta^2} \right]. \tag{3.28}$$

We have used that Q_2 is odd with respect to $y_2 = \delta/2$ in the slot, hence its behavior at infinity when $y_1 \to +\infty$. From the matching condition (3.18) with the exterior together with (3.15), we get

$$p^1(0^-, x_2, t) = \lim_{y_1 \to -\infty} \left(\mathsf{p}^1(\boldsymbol{y}, x_2, t) + y_1 \frac{\partial u^0}{\partial t}\Big|_{0^-} \right) = Q_*(x_2, t). \tag{3.29}$$

From the matching condition (3.20) with the first slot together with (3.11) and (3.23) which gives $\frac{\partial u^0}{\partial t}|_{0^-} = \frac{\partial u^0_{(1)}}{\partial t}|_{0^+} = -\delta \frac{\partial p^0}{\partial x_1}|_{0^+}$, we get

$$p^1(0^+, x_2, y_2 \in Y_{(1)}, t) = \lim_{y_1 \to +\infty} \left(\mathsf{p}^1(\boldsymbol{y}, x_2, t) + \frac{y_1}{\delta} \frac{\partial u^0}{\partial t}\Big|_{0^-} \right)$$
$$= -\mathcal{B} \frac{\partial u^0}{\partial t}\Big|_{0^-} + \frac{\partial p^0}{\partial x_2}\Big|_{0^-} (y_{(1)} - y_2) + Q_*(x_2, t).$$

Using (3.12) (since $p^0|_{0^-} = p^0_{(1)}|_{0^+}$), we deduce

$$p^1_{(1)}(0^+, x_2, t) = -\mathcal{B} \frac{\partial u^0}{\partial t}\Big|_{0^-} + Q_*(x_2, t). \tag{3.30}$$

Finally, subtracting (3.29) to (3.30) we get the jump conditions on the pressure field

$$p^1_{(1)}(0^+, x_2, t) - p^1(0^-, x_2, t) = -\mathcal{B} \frac{\partial u^0}{\partial t}\Big|_{0^-}. \tag{3.31}$$

By conducting the same analysis at the other extremity $x_1 = \ell$ of the slot, we obtain

$$p^1(\ell^+, x_2, t) - p^1_{(N)}(\ell^-, x_2, t) = -\mathcal{B} \frac{\partial u^0}{\partial t}\Big|_{\ell^+}. \tag{3.32}$$

Jump condition on the flow rate. We start from the divergence relation on $\mathbf{u}^1$ in (3.17) that we integrate over the truncated domain $\mathcal{Y}^*$ after taking the time derivative, specifically we get

$$\int_{\mathcal{Y}^*} \left(\mathrm{div}_y \frac{\partial \mathbf{u}^1}{\partial t} + \frac{\partial^2 \mathsf{v}^0}{\partial t \partial x_2} + \frac{\partial^2 \mathsf{p}^0}{\partial t^2} \right) \mathrm{d}\boldsymbol{y} = 0. \tag{3.33}$$

We evaluate separately the three contributions in the integral in (3.33). First, since p^0 is constant in $\mathcal{Y}$, see (3.22), we have

$$\int_{\mathcal{Y}^*} \frac{\partial^2 \mathsf{p}^0}{\partial t^2} \, \mathrm{d}\boldsymbol{y} = (1+\delta) y_1^* \frac{\partial^2 p^0}{\partial t^2}\Big|_{0^-}. \tag{3.34}$$

Next, using the divergence theorem and the matching conditions (3.18)-(3.20) written for the velocity as well as the definitions (3.5) of the flow rate, we have the asymptotic estimate

$$\int_{\mathcal{Y}^*} \mathrm{div}_y \frac{\partial \mathbf{u}^1}{\partial t} \, \mathrm{d}\boldsymbol{y} = \frac{\partial u^1_{(1)}}{\partial t}\Big|_{0^+} - \frac{\partial u^1}{\partial t}\Big|_{0^-} + y_1^* \frac{\partial^2 u^0_{(1)}}{\partial t \partial x_1}\Big|_{0^+} + y_1^* \frac{\partial^2 u^0}{\partial t \partial x_1}\Big|_{0^-} + o(1) \tag{3.35}$$

where $o(1)$ are vanishing terms as $y_1^* \to +\infty$. Adding the two contributions (3.34) and (3.35) and using mass balance equations (3.11) and (3.15), we get

$$\int_{\mathcal{Y}^*} \left(\mathrm{div}_y \frac{\partial \mathbf{u}^1}{\partial t} + \frac{\partial^2 \mathsf{p}^0}{\partial t^2} \right) \mathrm{d}\boldsymbol{y} = \frac{\partial u^1_{(1)}}{\partial t}\Big|_{0^+} - \frac{\partial u^1}{\partial t}\Big|_{0^-} - y_1^* \frac{\partial^2 v^0}{\partial t \partial x_2}\Big|_{0^-} + o(1). \tag{3.36}$$

The remaining term of the integral (3.33) can be expressed using (3.24) as

$$\int_{\mathcal{Y}^*} \frac{\partial^2 \mathsf{v}^0}{\partial t \partial x_2} \, \mathrm{d}\boldsymbol{y} = -(1+\delta) y_1^* \frac{\partial^2 p^0}{\partial x_2^2}\Big|_{0^-} - \int_{\mathcal{Y}^*} \frac{\partial^2 \mathsf{p}^1}{\partial x_2 \partial y_2} \, \mathrm{d}\boldsymbol{y}. \tag{3.37}$$

The last integral can be made explicit using (3.25) to get

$$\int_{\mathcal{Y}^*} \frac{\partial^2 \mathsf{p}^1}{\partial x_2 \partial y_2}\,\mathrm{d}\boldsymbol{y} = \frac{\partial^2 p^0}{\partial x_2^2}\Big|_{0^-}\left(\int_{\mathcal{Y}^*\cap\mathcal{Y}^-}\frac{\partial Q_2}{\partial y_2}\,\mathrm{d}\boldsymbol{y} + \int_{\mathcal{Y}^*\cap\mathcal{Y}^+}\left(\frac{\partial Q_2}{\partial y_2}+1\right)\,\mathrm{d}\boldsymbol{y} - \delta y_1^*\right)$$

$$- \frac{\partial^2 u^0}{\partial t \partial x_2}\Big|_{0^-}\int_{\mathcal{Y}^*}\frac{\partial Q_1}{\partial y_2}\,\mathrm{d}\boldsymbol{y} + o(1). \tag{3.38}$$

Note that due to periodicity conditions in $\mathcal{Y}^-$, we have $\int_{\mathcal{Y}^*\cap\mathcal{Y}^-}\frac{\partial Q_i}{\partial y_2}\,\mathrm{d}\boldsymbol{y} = 0$ for $i = 1, 2$. One can also remark that the loading being in the direction $\boldsymbol{e}_1$ for Q_1, the solution is symmetric with respect to $y_2 = \delta/2$ in the slot and hence we have $\int_{\mathcal{Y}^*\cap\mathcal{Y}^+}\frac{\partial Q_1}{\partial y_2}\,\mathrm{d}\boldsymbol{y} = 0$. Finally, introducing the boundary layer corrector

$$\mathcal{C} = \int_{\mathcal{Y}^+}\left(\frac{\partial Q_2}{\partial y_2}+1\right)\,\mathrm{d}\boldsymbol{y}, \tag{3.39}$$

and adding (3.36) to (3.37) with the use of (3.38), we get

$$\frac{\partial}{\partial t}\left(u^1_{(1)}(0^+, x_2, t) - u^1(0^-, x_2, t)\right) = \mathcal{C}\frac{\partial^2 p^0}{\partial x_2^2}(0^-, x_2, t).$$

To get rid of the time derivative, we introduce the auxiliary velocity field $W_0(x_2, t)$ which allows us to express the jump condition on the normal velocity at first order as

$$u^1_{(1)}(0^+, x_2, t) - u^1(0^-, x_2, t) = -\mathcal{C}\frac{\partial W_0}{\partial x_2}, \quad \frac{\partial W_0}{\partial t}(x_2, t) = -\frac{\partial p^0}{\partial x_2}(0^-, x_2, t), \tag{3.40}$$

By conducting the same analysis at the exit of the crystaline region, we get

$$u(\ell^+, x_2, t) - u^1_{(N)}(\ell^-, x_2, t) = -\mathcal{C}\frac{\partial W_N}{\partial x_2}, \quad \frac{\partial W_N}{\partial t}(x_2, t) = -\frac{\partial p^0}{\partial x_2}(\ell^+, x_2, t). \tag{3.41}$$

3.4. Analysis at the junctions. We shall now derive the effective jump conditions applying between two consecutive slots at a turning region. We notice that a similar analysis has been conducted in [6, 3]. For the sake of conciseness, we shall consider a turning region close to $x_1 = 0$, that is to say between the n-th and the $(n+1)$-th slot with n even. The conditions for the turning region on the opposite side near $x_1 = \ell$ can be deduced by mirroring the analysis. We also notice that the analysis is very similar but not identical to that developed in the preceding section; to avoid multiple references to this previous analysis, we simply repeat below the exercice.

3.4.1. Setting of the asymptotic procedure. With $y_{(n)}$ and $Y_{(n)}$ defined by (3.4), we define the representative cell $\mathcal{Y}_c$ of the turning region (see figure 6), using the rescaled space variable $\boldsymbol{y} = \boldsymbol{x}/\varepsilon$, as the semi-infinite region

$$\mathcal{Y}_c = (\gamma, \gamma+\eta)\times(y_{(n)} - \delta/2, y_{(n+1)} + \delta/2) \cup (\gamma+\eta, +\infty)\times(Y_{(n)} \cup Y_{(n+1)}).$$

In this region, we use the following asymptotic expansions

$$p^\varepsilon = \sum_{i\geqslant 0}\varepsilon^i \mathsf{p}^i_c(x_2, \boldsymbol{y}, t), \qquad \boldsymbol{u}^\varepsilon = \sum_{i\geqslant 0}\varepsilon^i \mathbf{u}^i_c(x_2, \boldsymbol{y}, t). \tag{3.42}$$

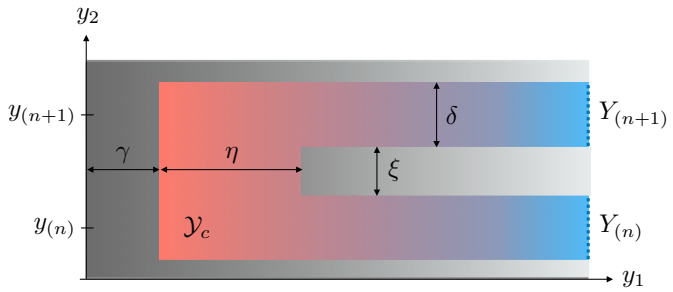

FIG. 6. *The representative cell $\mathcal{Y}_c$ at a turn connecting two consecutive slots (red region).*

Injecting (3.42) in the governing equations (3.2), we get at the leading orders

$$\begin{cases} \mathrm{div}_y \mathbf{u}_c^0 = 0, \quad \mathrm{div}_y \mathbf{u}_c^1 + \partial_{x_2} \mathsf{v}_c^0 + \dfrac{\partial \mathsf{p}_c^0}{\partial t} = 0, \\ 0 = \boldsymbol{\nabla}_y \mathsf{p}_c^0, \quad \dfrac{\partial \mathbf{u}_c^0}{\partial t} = -\dfrac{\partial \mathsf{p}_c^0}{\partial x_2} \boldsymbol{e}_2 - \boldsymbol{\nabla}_y \mathsf{p}_c^1. \\ \mathbf{u}_c^0 \cdot \boldsymbol{n}_{|\Gamma_c} = \mathbf{u}_c^1 \cdot \boldsymbol{n}_{|\Gamma_c} = 0, \end{cases} \tag{3.43}$$

where Γ_c denotes the part of the boundary $\mathcal{Y}_c$ associated to the rigid walls. The matching conditions between the inner expansions and the outer expansions (3.3) far in the slots can be derived using the same procedure as in the preceding §3.3.1. For the pressure, they read

$$\begin{aligned} p^0(0^+, \boldsymbol{\alpha}_i) &= \lim_{y_1 \to +\infty} \mathsf{p}_c^0(y_1, \boldsymbol{\alpha}_i), \\ p^1(0^+, \boldsymbol{\alpha}_i) &= \lim_{y_1 \to +\infty} \left(\mathsf{p}_c^1(y_1, \boldsymbol{\alpha}_i) - y_1 \frac{\partial p^0}{\partial x_1}(0^+, \boldsymbol{\alpha}_i) \right), \end{aligned} \tag{3.44}$$

with the notation $\boldsymbol{\alpha}_i = (y_2 \in Y_{(i)}, x_2, t)$ for $i = \{n, n+1\}$. The same matching conditions on the velocity are obtained by replacing formally p by $\boldsymbol{u}$ and p_c by $\mathbf{u}_c$ in (3.44).

3.4.2. The continuity conditions at order 0. At the dominant order, we get from (3.43) that p_c^0 is independent of $\boldsymbol{y}$, hence we obtain from the matching condition (3.44) together with the result (3.9) set in the bulk that

$$p_{(n+1)}^0(0^+, x_2, t) = \mathsf{p}_c^0(x_2, \boldsymbol{y}, t) = p_{(n)}^0(0^+, x_2, t), \tag{3.45}$$

which translates in the continuity of the pressure between two consecutive slots. Next, by integrating the divergence free equation in (3.43) over the subset domain $\mathcal{Y}_c^* \subset \mathcal{Y}$, truncated at $y_1 = \pm y_1^*$ with $y_1^* \gg 1$, and eliminating the boundary terms associated to the Neumann boundary conditions on the rigid walls, we obtain

$$\int_{Y_{(n)}} \mathsf{u}_c^0(x_2, y_1^*, y_2, t)\, y_2 + \int_{Y_{(n+1)}} \mathsf{u}_c^0(x_2, y_1^*, y_2, t)\, \mathrm{d}y_2 = 0.$$

Passing to the limit when $y_1^* \to +\infty$ and using the matching condition (3.44) (written for the velocity) together with the definitions of the flow rate (3.5) in the bulk, we obtain a jump condition on the flow rate

$$u_{(n+1)}^0(0^+, x_2, t) + u_{(n)}^0(0^+, x_2, t) = 0. \tag{3.46}$$

At the dominant order, we recover the continuity conditions on the pressure and on the flowrate.

3.4.3. The jump conditions at order 1.

Jump condition on the pressure. From (3.43), the problem set for the couple $(\mathsf{p}_c^1, \mathbf{u}_c^0)$ is given by

$$\begin{cases} \dfrac{\partial \mathbf{u}_c^0}{\partial t} = -\dfrac{\partial p_{(n)}^0}{\partial x_2}\Big|_{0^+} \boldsymbol{e}_2 - \boldsymbol{\nabla}_y \mathsf{p}_c^1 \ , \quad \mathrm{div}_y \mathbf{u}_c^0 = \mathbf{0} \ , \quad \mathbf{u}_c^0 \cdot \boldsymbol{n}_{|\Gamma_c} = 0 \ , \\ \lim\limits_{y_1 \to +\infty} \dfrac{\partial \mathbf{u}_c^0}{\partial t}(y_1, y_2 \in Y_{(n)}, x_2, t) = \dfrac{1}{\delta} \dfrac{\partial u_{(n)}^0}{\partial t}\Big|_{0^+} \boldsymbol{e}_1, \\ \lim\limits_{y_1 \to +\infty} \dfrac{\partial \mathbf{u}_c^0}{\partial t}(y_1, y_2 \in Y_{(n+1)}, x_2, t) = -\dfrac{1}{\delta} \dfrac{\partial u_{(n)}^0}{\partial t}\Big|_{0^+} \boldsymbol{e}_1. \end{cases} \tag{3.47}$$

The above formulation has been obtained using i) (3.46) used to express the limit when $y_1 \to +\infty$ in terms of $\frac{\partial u_{(n)}^0}{\partial t}|_{0^+}$ only, ii) that the vertical velocity v^0 is zero in the slots from (3.10), iii) the continuity of the pressure in (3.45) which shows that $\frac{\partial \mathsf{p}_c^0}{\partial x_2} = \frac{\partial p_{(n)}^0}{\partial x_2}|_{0^+}$. The solution of (3.47) can now be expressed as a linear combination of the two macroscopic fields $\frac{\partial p_{(n)}^0}{\partial x_2}|_{0^+}$ and $\frac{\partial u_{(n)}^0}{\partial t}|_{0^+}$ (which are independent of $\boldsymbol{y}$), namely we use

$$\mathsf{p}_c^1(x_2, \boldsymbol{y}, t) = \frac{\partial p_{(n)}^0}{\partial x_2}\Big|_{0^+} (y_{(n)} - y_2) - \frac{\partial u_{(n)}^0}{\partial t}\Big|_{0^+} Q^{(n)}(\boldsymbol{y}) + Q_*^{(n)}(x_2, t), \tag{3.48}$$

with $Q^{(n)}(\boldsymbol{y})$ being solutions to the elementary problems

$$\begin{cases} \Delta_y Q^{(n)} = 0 \ \text{ in } \mathcal{Y}_c, \quad \boldsymbol{\nabla}_y Q^{(n)} \cdot \boldsymbol{n}_{|\Gamma_c} = 0, \\ \lim\limits_{y_1 \to +\infty} \boldsymbol{\nabla}_y Q^{(n)}(y_1, y_2 \in Y_{(n)}) = \dfrac{\boldsymbol{e}_1}{\delta}, \quad \lim\limits_{y_1 \to +\infty} \boldsymbol{\nabla}_y Q^{(n)}(y_1, y_2 \in Y_{(n+1)}) = -\dfrac{\boldsymbol{e}_1}{\delta}. \end{cases} \tag{3.49}$$

The asymptotic behavior of $Q^{(n)}$ at infinity is given by

	$\lim\limits_{y_2 \in Y_{(n)}, y_1 \to +\infty}$	$\lim\limits_{y_2 \in Y_{(n+1)}, y_1 \to +\infty}$
$Q^{(n)}$	$\dfrac{y_1}{\delta}$	$-\dfrac{y_1}{\delta} - \mathcal{D}^*$

(3.50)

The elementary problem (3.49), as those in (3.26), corresponds to a potential flow problem, for a perfect fluid flowing in a curved portion of a rigid duct; however, as far as we know, explicit expression of the blockage coefficient $\mathcal{D}^*$ is not available in the literature. We can now express jump conditions at the first order. For that, we pass to the limit in (3.48) with the help of the asymptotic behavior (3.50), and then make use of the matching conditions (3.44) together with the form (3.12) of the pressure p^1 in the slots. This leads to

$$\begin{aligned} p_{(n+1)}^1(0^+, x_2, t) &= (y_{(n)} - y_{(n+1)}) \frac{\partial p_{(n)}^0}{\partial x_2}\Big|_{0^+} - \mathcal{D}^* \frac{\partial u_{(n+1)}^0}{\partial t}\Big|_{0^+} + Q_*^{(n)}(x_2, t), \\ p_{(n)}^1(0^+, x_2, t) &= Q_*^{(n)}(x_2, t). \end{aligned}$$

Noticing that $y_{(n+1)} - y_{(n)} = \delta + \xi$, we deduce the jump condition on the pressure at the junction between each slot

$$p^1_{(n+1)}(0^+, x_2, t) - p^1_{(n)}(0^+, x_2, t) = -\mathcal{D}^* \frac{\partial u^0_{(n+1)}}{\partial t}\Big|_{0^+} - (\delta + \xi)\frac{\partial p^0_{(n)}}{\partial x_2}\Big|_{0^+}. \tag{3.51}$$

Jump condition on the velocity. We start from the divergence relation on $\mathbf{u}^1$ in (3.43) that we integrate over the truncated domain $\mathcal{Y}_c^*$ after taking the time derivative. This reads

$$\int_{\mathcal{Y}_c^*} \left(\mathrm{div}_y \frac{\partial \mathbf{u}^1_c}{\partial t} + \frac{\partial^2 \mathsf{v}^0_c}{\partial t \partial x_2} + \frac{\partial^2 \mathsf{p}^0_c}{\partial t^2} \right) \mathrm{d}\boldsymbol{y} = 0. \tag{3.52}$$

We evaluate below the three contributions in the integral in (3.52). First, since p^0_c is constant in $\mathcal{Y}_c$, see (3.45), we have

$$\int_{\mathcal{Y}_c^*} \frac{\partial^2 \mathsf{p}^0_c}{\partial t^2}\, \mathrm{d}\boldsymbol{y} = (2\delta(y_1^* - \gamma) + \xi\eta)\, \frac{\partial^2 p^0_{(n)}}{\partial t^2}\Big|_{0^+}. \tag{3.53}$$

Next, using the divergence theorem and the matching conditions (3.44) written for the velocity, we have the asymptotic estimate

$$\int_{\mathcal{Y}_c^*} \mathrm{div}_y \frac{\partial \mathbf{u}^1_c}{\partial t}\, \mathrm{d}\boldsymbol{y} = \frac{\partial u^1_{(n+1)}}{\partial t}\Big|_{0^+} + \frac{\partial u^1_{(n)}}{\partial t}\Big|_{0^+} + y_1^* \frac{\partial^2 u^0_{(n+1)}}{\partial t \partial x_1}\Big|_{0^+} + y_1^* \frac{\partial^2 u^0_{(n)}}{\partial t \partial x_1}\Big|_{0^+} + o(1), \tag{3.54}$$

where $o(1)$ are vanishing terms as $y_1^* \to +\infty$. Adding the two contributions (3.53) and (3.54) and using mass balance equations (3.11), we get

$$\int_{\mathcal{Y}_c^*} \left(\mathrm{div}_y \frac{\partial \mathbf{u}^1_c}{\partial t} + \frac{\partial^2 \mathsf{p}^0_c}{\partial t^2} \right) \mathrm{d}\boldsymbol{y} = \frac{\partial u^1_{(n+1)}}{\partial t}\Big|_{0^+} + \frac{\partial u^1_{(n)}}{\partial t}\Big|_{0^+} + (\xi\eta - 2\delta\gamma)\frac{\partial^2 p^0_{(n)}}{\partial t^2}\Big|_{0^+} + o(1). \tag{3.55}$$

The remaining term of the integral (3.52) can be further simplified using (3.47), namely

$$\int_{\mathcal{Y}_c^*} \frac{\partial^2 \mathsf{v}^0_c}{\partial t \partial x_2}\, \mathrm{d}\boldsymbol{y} = \frac{\partial^2 u^0_{(n)}}{\partial t \partial x_2}\Big|_{0^+} \int_{\mathcal{Y}_c^*} \frac{\partial Q^{(n)}}{\partial y_2}\, \mathrm{d}\boldsymbol{y} \tag{3.56}$$

with the integral on the right-hand side being explicit. Indeed, integrating by part of (3.49) after a multiplication by y_2 gives

$$0 = \int_{\mathcal{Y}_c} y_2 \Delta_y Q^{(n)}\, \mathrm{d}\boldsymbol{y} = \int_{\partial \mathcal{Y}_c} y_2 \boldsymbol{\nabla}_y Q^{(n)} \cdot \boldsymbol{n}\, \mathrm{d}\boldsymbol{y} - \int_{\mathcal{Y}_c} \frac{\partial Q^{(n)}}{\partial y_2}\, \mathrm{d}\boldsymbol{y}.$$

Eliminating the zero contribution in the boundary integral, on the rigid walls due to the Neumann boundary condition, it leaves only the contribution when $y_1 \to +\infty$

$$\int_{\partial \mathcal{Y}_c} y_2 \boldsymbol{\nabla}_y Q^{(n)} \cdot \boldsymbol{n}\, \mathrm{d}\boldsymbol{y} = \frac{1}{\delta}\int_{Y_{(n)}} y_2\, \mathrm{d}y_2 - \frac{1}{\delta}\int_{Y_{(n+1)}} y_2\, \mathrm{d}y_2 = -(\delta + \xi)$$

from which we deduce that $\int_{\mathcal{Y}_c} \frac{\partial Q^{(n)}}{\partial y_2}\, \mathrm{d}\boldsymbol{y} = -(\delta + \xi)$. Finally, adding (3.55) and (3.56), we find the jump condition at order 1 on the normal velocity

$$u^1_{(n+1)}(0^+, x_2, t) + u^1_{(n)}(0^+, x_2, t) = -(\xi\eta - 2\delta\gamma)\frac{\partial p^0_{(n)}}{\partial t}\Big|_{0^+} + (\delta + \xi)\frac{\partial u^0_{(n)}}{\partial x_2}\Big|_{0^+}. \tag{3.57}$$

3.5. Unique formation of the effective problem with curvilinear coordinate.

3.5.1. The curvilinear description. The effective problem derived from the asymptotic analysis in the slots can be rewritten *a posteriori* in a more intuitive form. It consists in using the curvillinear coordinate s that runs along the coiled slot. Specifically, s is defined over $(0, N\ell)$ with the mapping from the global frame, made of the N slots, to the curvilinear frame, made of a single path, given by

$$\begin{cases} (n, x_1) \mapsto s = \left(n - \frac{1}{2}\right)\ell + (-1)^n \left(\frac{\ell}{2} - x_1\right), \\ \{1, \dots, N\} \times (0, \ell) \mapsto (0, N\ell). \end{cases} \tag{3.58}$$

Expressing the one-dimensional wave equation (3.11) and (3.13) in terms of s gives

$$i \in \{0,1\}, \quad s \in (0, N\ell), \quad \frac{\partial U^i}{\partial t} + \delta \frac{\partial P^i}{\partial s} = 0, \qquad \frac{\partial U^i}{\partial s} + \delta \frac{\partial P^i}{\partial t} = 0, \tag{3.59}$$

where (P^i, U^i) are the pressure and flow rate variables set in the new frame and defined as

$$(P^i(s, x_2), U^i(s, x_2)) = (p^i_{(n)}(x_1, x_2), (-1)^n u^i_{(n)}(x_1, x_2)). \tag{3.60}$$

At the entrance and the exit of the crystalline region, at $s = 0$ and $s = N\ell$, the continuity conditions at order 0, (3.22) and (3.23), now read

$$\begin{cases} P^0|_{s=0^+} - p^0|_{x_1=0^-} = p^0|_{x_1=\ell^+} - P^0|_{s=(N\ell)^-} = 0, \\ U^0|_{s=0^+} - u^0|_{x_1=0^-} = U^0|_{x_1=\ell^+} - u^0|_{s=(N\ell)^-} = 0, \end{cases} \tag{3.61}$$

while the jump conditions at order 1, (3.31)-(3.32) and (3.40)-(3.41), are given by

$$\begin{cases} P^1|_{s=0^+} - p^1|_{x_1=0^-} = -\mathcal{B}\dfrac{\partial u^0}{\partial t}\Big|_{x_1=0^-}, \quad U^1|_{s=0^+} - u^1|_{x_1=0^-} = -\mathcal{C}\dfrac{\partial W_0}{\partial x_2}, \\ p^1|_{x_1=\ell^+} - P^1|_{s=(N\ell)^-} = -\mathcal{B}\dfrac{\partial u^0}{\partial t}\Big|_{x_1=\ell^+}, \quad u^1|_{x_1=\ell^+} - U^1|_{s=(N\ell)^-} = -\mathcal{C}\dfrac{\partial W_N}{\partial x_2}, \end{cases} \tag{3.62}$$

with (W_0, W_N) still given by (3.40) and (3.41).

Eventually, at the turning regions, the jump conditions (3.45) and (3.46) at order 0, (3.51) and (3.57) at order 1, now apply at $s = n\ell$ with $n \in \{1, \dots, N-1\}$ and read

$$\begin{cases} [\![P^0]\!] = [\![U^0]\!] = 0, \\ [\![P^1]\!] = -\mathcal{D}^* \dfrac{\partial U^0}{\partial t}\Big|_{n\ell} - (\delta + \xi)\dfrac{\partial P^0}{\partial x_2}\Big|_{n\ell}, \\ [\![U^1]\!] = -(\xi\eta - 2\delta\gamma)\dfrac{\partial P^0}{\partial t}\Big|_{n\ell} - (\delta + \xi)\dfrac{\partial U^0}{\partial x_2}\Big|_{n\ell}. \end{cases} \tag{3.63}$$

3.5.2. The unique formulation. The last step in the construction of the effective model is to gather the contributions $(p^0, P^0, \boldsymbol{u}^0, U^0)$ at order 0 and $(p^1, P^1, \boldsymbol{u}^1, U^1)$ at order 1 into a unique problem. In the surrounding air we introduce

$$p = p^0 + \varepsilon p^1 \quad \text{and} \quad \boldsymbol{u} = \boldsymbol{u}^0 + \varepsilon \boldsymbol{u}^1, \tag{3.64}$$

and inside the equivalent metacrystalline region, we introduce the pressure and flow rate fields (in the curvilinear frame)

$$P = P^0 + \varepsilon P^1 \quad \text{and} \quad U = U^0 + \varepsilon U^1. \tag{3.65}$$

Using (3.15) and (3.59), it is straightforward to deduce the final effective wave equations (2.2)-(2.3) after using the dimensionalization procedure (3.1). The derivation of the unique formulation of the jump conditions is more involved as it requires the introduction of mean quantities. At the entry of the metacrystalline region, in virtue of the continuity of the flow rate (3.61) at order 0 combined with (3.64)-(3.65), we have

$$\frac{\partial u^0}{\partial t}\Big|_{x_1=0^-} = \frac{1}{2}\left(\frac{\partial u}{\partial t}\Big|_{x_1=0^-} + \frac{\partial U}{\partial t}\Big|_{s=0^+}\right) + O(\varepsilon). \tag{3.66}$$

Now, summing the contributions (3.61) at order 0 and (3.62) at order 1 on the pressure together with (3.66), we finally get the jump condition on the pressure (2.6) at the entry (up to the second order in ε). Next the continuity equation on the pressure (3.61) implies that (3.40) gives

$$\frac{\partial W_0}{\partial t} = -\frac{1}{2}\left(\frac{\partial p}{\partial x_2}\Big|_{x_1=0^-} + \frac{\partial P}{\partial x_2}\Big|_{s=0^+}\right) + O(\varepsilon), \tag{3.67}$$

which allows to deduce from (3.61) and (3.62) the jump condition on the flow rate (2.6) at the entry (up to the second order in ε). The same exact procedure can be applied to get the final jump conditions at the exit of the metacrystalline region.

Getting the final jump conditions at each junction needs to introduce the enlargement of the interface due to the finite size of the turning region (at order 1). This is done in order to ensure stability of the model which requires that a positive definite energy can be defined; examples can be found in [4, 13] and the positivity will be proven in the forthcoming §4. To do this, we aim to express the jump conditions, when going from the slot n to the slot $(n+1)$, in terms of s values $s = n\ell - e$ and $s = n\ell + e$ (with $e = (\eta + \gamma)\varepsilon$). By doing a Taylor expansion as $\varepsilon \ll 1$ of the continuity conditions (3.63) on the pressure field and using (3.59), it can be shown that

$$P^0|_{s=n\ell+e} - P^0|_{s=n\ell-e} = -\varepsilon\frac{2}{\delta}(\eta+\gamma)\frac{\partial\langle U\rangle}{\partial t} + O(\varepsilon^2), \tag{3.68}$$

with the mean operation defined as

$$\langle f\rangle = \frac{1}{2}\left(f|_{s=n\ell+e} + f|_{s=n\ell-e}\right). \tag{3.69}$$

Similarly at the next order, by doing a Taylor expansion on the first order jump condition (3.63) on the pressure, we have

$$P^1|_{s=n\ell+e} - P^1|_{s=n\ell-e} = -\mathcal{D}^*\frac{\partial\langle U\rangle}{\partial t} - (\delta+\xi)\frac{\partial\langle P\rangle}{\partial x_2} + O(\varepsilon). \tag{3.70}$$

Now multiplying (3.70) by ε and adding the contribution (3.68), we obtain the desired jump conditions (2.5) at the junction on the pressure field (valid up to the second order in ε) with

$$\mathcal{D} = \mathcal{D}^* + \frac{2(\eta+\gamma)}{\delta}. \tag{3.71}$$

The unique formulation of the jump condition on the flow rate at the junction is obtained similarly. We first enlarged the continuity condition (3.63) with a Taylor expansion to get

$$U^0|_{s=n\ell+e} - U^0|_{s=n\ell-e} = -2\delta(\eta+\gamma)\varepsilon\frac{\partial\langle P\rangle}{\partial t} + O(\varepsilon^2), \tag{3.72}$$

with $\langle P\rangle$ defined by (3.69). We proceed similarly with the jump condition at the first order to get

$$U^1|_{s=n\ell+e} - U^1|_{s=n\ell-e} = -(\xi\eta - 2\delta\gamma)\frac{\partial\langle P\rangle}{\partial t} - (\delta+\xi)\frac{\partial\langle U\rangle}{\partial x_2} + O(\varepsilon). \tag{3.73}$$

Now multiplying (3.73) by ε and adding the contribution (3.72), we obtain the desired jump conditions (2.5) (valid up to the second order in ε).

4. Energetic properties.

4.1. Energy balance of the effective model. We consider a rectangular domain $\Omega = (-L_1, L_1)\times(-L_2, L_2)$ with $L_1 > \ell$ so that Ω contains the crystalline region. In the direct problem given by (2.1), the classical energy balance equation is given by

$$\frac{\mathrm{d}\mathcal{E}_{\mathrm{b}}}{\mathrm{d}t} + \int_{\partial\Omega} \boldsymbol{\pi}\cdot\boldsymbol{n}\,\mathrm{d}\boldsymbol{x} = 0, \qquad \text{with} \quad \mathcal{E}_{\mathrm{b}} = \frac{1}{2}\int_{\Omega}\left(\chi_{\mathrm{a}}p^2 + \rho_{\mathrm{a}}|\boldsymbol{u}|^2\right)\,\mathrm{d}\boldsymbol{x},$$

where $\mathcal{E}_{\mathrm{b}}$ is the acoustic bulk energy and $\boldsymbol{\pi} = p\boldsymbol{u}$ the Poynting vector that accounts for the flux energy throughout the boundary $\partial\Omega$. A similar energy balance can be obtained for the effective model (2.2)-(2.6). Specifically, it involves four contributions to the energy and reads

$$\frac{\mathrm{d}}{\mathrm{d}t}\left[\mathcal{E}_{\mathrm{b}}^{\mathrm{air}} + \mathcal{E}_{\mathrm{b}}^{\mathrm{slot}} + \mathcal{E}_{\mathrm{s}}^{\mathrm{in/out}} + \mathcal{E}_{\mathrm{s}}^{\mathrm{turn}}\right] + \int_{\partial\Omega}\boldsymbol{\pi}\cdot\boldsymbol{n}\,\mathrm{d}\boldsymbol{x} = 0. \tag{4.1}$$

The bulk energy $\mathcal{E}_{\mathrm{b}}^{\mathrm{air}}$ is the standard energy stored in Ω/Ω^*, the region of the surrounding air, with $\Omega^* = (0,\ell)\times(-L_2, L_2) \subset \Omega$, namely

$$\mathcal{E}_{\mathrm{b}}^{\mathrm{air}} = \frac{1}{2}\int_{\Omega/\Omega^*}\left(\chi_{\mathrm{a}}p^2 + \rho_{\mathrm{a}}|\boldsymbol{u}|^2\right)\,\mathrm{d}\boldsymbol{x}. \tag{4.2}$$

The bulk energy $\mathcal{E}_{\mathrm{b}}^{\mathrm{slot}}$ is the effective energy stored in the straight slots. Expressed by means of the curvilinear coordinate, it reads:

$$\mathcal{E}_{\mathrm{b}}^{\mathrm{slot}} = \frac{1}{2}\sum_{n=0}^{N-1}\int_{-L_2}^{L_2}\int_{s_n^+}^{s_{n+1}^-}\left(\chi_{\mathrm{a}}\delta P^2 + \frac{\rho_{\mathrm{a}}}{\delta}U^2\right)\,\mathrm{d}s\,\mathrm{d}x_2. \tag{4.3}$$

The surface energy $\mathcal{E}_{\mathrm{s}}^{\mathrm{in/out}}$ is the sum of the effective energies stored in the boundary layers at the entry/exit of the coiled slot and it reads

$$\mathcal{E}_{\mathrm{s}}^{\mathrm{in/out}} = \frac{1}{2}\sum_{n\in\{0,N\}}\int_{-L_2}^{L_2}\rho_{\mathrm{a}}\left(h\mathcal{C}W_n^2 + h\mathcal{B}\langle U\rangle_n^2\right)\,\mathrm{d}x_2. \tag{4.4}$$

Finally the surface energy $\mathcal{E}_{\rm s}^{\rm turn}$ is the sum of the effective energies stored in the boundary layers at each turning region between two consecutive slots; it reads

$$\mathcal{E}_{\rm s}^{\rm turn} = \frac{1}{2}\sum_{n=1}^{N-1}\int_{-L_2}^{L_2}\left(\chi_{\rm a}h(2\delta+\xi)\eta\langle P\rangle_n^2 + \rho_{\rm a}h\mathcal{D}\langle U\rangle_n^2\right)\,{\rm d}x_2. \tag{4.5}$$

A proof of the positivity of the effective coefficients $(\mathcal{B},\mathcal{C},\mathcal{D})$ is given in the supplementary material (SM1). This ensures the positivity of the surface energies, hence avoiding numerical instabilities in the time domain, see [5] for a detailed analysis of such issue.

4.2. Derivation of the energy balance. Multiplying in (2.3) the momentum balance and the mass balance by $\frac{\rho_{\rm a}}{\delta}U$ and P, respectively (for each segment $s \in (s_n^+, s_{n+1}^-)$ with $n \in \{0,\dots,N-1\}$), and adding the two contributions, we get

$$s \in (s_n^+, s_{n+1}^-), \qquad \chi_{\rm a}\delta P\frac{\partial P}{\partial t} + \frac{\rho_{\rm a}}{\delta}U\frac{\partial U}{\partial t} + \frac{\partial (PU)}{\partial s} = 0. \tag{4.6}$$

Similarly in the air we have

$$\chi_{\rm a}p\frac{\partial p}{\partial t} + \rho_{\rm a}\boldsymbol{u}\cdot\frac{\partial \boldsymbol{u}}{\partial t} + {\rm div}(p\boldsymbol{u}) = 0. \tag{4.7}$$

To obtain a balance of energy, we start with the energy stored in the surrounding air by integrating (4.7) over Ω/Ω^*, which makes (4.2) appear. Next we integrate (4.6) over $x_2 \in (-L_2, L_2)$ and each segment (s_n^+, s_{n+1}^-), which makes (4.3) appear. Summing the two contributions, and using the divergence theorem, we get

$$\frac{\rm d}{{\rm d}t}\left[\mathcal{E}_{\rm b}^{\rm air} + \mathcal{E}_{\rm b}^{\rm slot}\right] - \sum_{n=0}^{N}\int_{-L_2}^{L_2}[\![PU]\!]_n\,{\rm d}x_2 + \int_{\partial\Omega}\boldsymbol{\pi}\cdot\boldsymbol{n}\,{\rm d}\boldsymbol{x} = 0,$$

with $\mathcal{E}_{\rm b}^{\rm air}$ and $\mathcal{E}_{\rm b}^{\rm slot}$ given by (4.2)-(4.3). The terms associated to the surface energies appear as we have the identity $[\![PU]\!]_n = [\![P]\!]_n\langle U\rangle_n + \langle P\rangle_n[\![U]\!]_n$. Specifically, by using the jump conditions, we get for $n = 0$ or N,

$$[\![PU]\!]_n = -\frac{1}{2}\frac{\rm d}{{\rm d}t}\rho_{\rm a}\left(h\mathcal{C}W_n^2 + h\mathcal{B}\langle U\rangle_n^2\right) - h\mathcal{C}\frac{\partial(\langle P\rangle_n W_n)}{\partial x_2}, \tag{4.8}$$

and, for $1 \le n \le (N-1)$,

$$[\![PU]\!]_n = -\frac{1}{2}\frac{\rm d}{{\rm d}t}\left(\chi_{\rm a}h(2\delta+\xi)\eta\langle P\rangle_n^2 + \rho_{\rm a}h\mathcal{D}\langle U\rangle_n^2\right) - h(\delta+\xi)\frac{\partial(\langle P\rangle_n\langle U\rangle_n)}{\partial x_2}. \tag{4.9}$$

We obtain the surface energies (4.4)-(4.5) after integration along x_2 of (4.9)-(4.8) (up to some flux terms at the edges of the crystalline region at $x_2 = \pm L_2$ and associated to the integration of the last term in (4.9) and (4.8). These contributions will be left out of the present analysis).

5. Validation of the effective model. In this section, we inspect the validity of our effective model at order 1 by comparing it to a numerical reference solution (details on the numerics -a multimodal method- are provided in the SM2.1). We also take the opportunity to compare this model with the one obtained at order 0, which,

as mentioned earlier, neglects the effects of boundary layers at the turning regions and at the extremities of the labyrinth. We consider the following geometry: zero wall thickness $\xi = \gamma = 0$ with $\ell = 2h$, h/N the length and width of the slot ($\delta = 1/N$ with $N = 7$) and $\eta h = 0.01h$ the width of the turning regions. The elementary problems (3.26) and (3.49) have been solved numerically in this configuration (using multimodal methods, see SM2.1) and the non-dimensional effective parameters $(\mathcal{B}, \mathcal{C}, \mathcal{D})$ entering the jump conditions (2.5) and (2.6) have been deduced (they are defined in (3.27), (3.39) and (3.50) along with (3.71)). We obtain $\mathcal{B} = 0.4982$ (in agreement with (3.28)), $\mathcal{C} = 0.0033$ and $\mathcal{D} = 0.4196/\delta$.

To begin with, we consider an incident plane wave in the harmonic regime with time dependence $e^{-i\omega t}$ at normal incidence (the case of oblique incidence is considered in SM2.2). Outside the metacrystal slab, the solution of the effective model reads

$$p(x_1, \omega) = \begin{cases} e^{ikx_1} + r(\omega)e^{-ikx_1}, & x_1 \in (-\infty, 0), \\ t(\omega)e^{ik(x_1-\ell)}, & x_1 \in (\ell, \infty). \end{cases} \tag{5.1}$$

We notice that the above solution holds for the actual problem far enough the slab where the evanescent fields can be neglected. Next, by solving (2.2)-(2.4) along with the jump conditions (2.5) and (2.6), we obtain the solution inside the slab and explicit values of (r, t) in (5.1) (see SM2.2). We report in figure 7(a) the transmission coefficient $t(\omega)$ obtained numerically for $\varepsilon = \omega h/c \in (0, 4.5)$ (below the threshold for the appearance of higher orders of diffraction at $\omega h/c = 2\pi$).

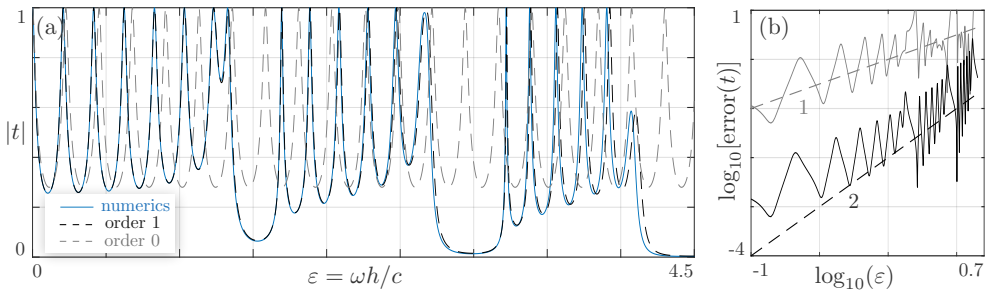

FIG. 7. *(a) Transmission coefficient $|t|$ against dimensionless frequency $\omega h/c$. (b) Relative errors of the models, in log-log representation, at orders 0 (grey, slope 1) and 1 (black, slope 2).*

The prediction of our model at order 1 is shown by black dashed lines and, for comparison, that of the model at order 0 by grey dashed lines (obtained by setting $\mathcal{B} = \mathcal{C} = \mathcal{D} = 0$). The relative errors $|t - t_{\text{num}}|/|t_{\text{num}}|$ against ε are reported in figure 7(b); they show that the model at order n, $n = 0, 1$, is accurate up to terms $O(\varepsilon^{n+1})$ as expected. More importantly in practice, we note that the order 1 model remains accurate over a wide range of frequencies that covers several perfect transmissions (at Fabry-Pérot resonances) and large transmission dips (at Bragg band-gaps). The lack of accuracy of the model at order 0 is visible as it slightly overestimates the Fabry-Pérot resonances and more critically, it ignores the Bragg band-gaps.

We now move on to the time-domain and consider an incident Gaussian pulse at

normal incidence, namely

$$p^{\rm inc}(x_1,t) = s\left(t - x_1/c\right), \quad \text{where} \quad s(t) = e^{-(t/\tau)^2}, \tag{5.2}$$

with τ the width of the Gaussian. The pressure field is obtained by solving the problem in the harmonic regime and applying Fourier transforms,

$$p(x_1,t) = \begin{cases} p^{\rm inc}(x_1,t) + 2\Re\left[\displaystyle\int_0^\infty \hat{s}(\omega) r(\omega)\, e^{-i\omega(t+x_1/c)}\, \mathrm{d}\omega\right], & x_1 \in (-\infty, 0), \\ 2\Re\left[\displaystyle\int_0^\infty \hat{s}(\omega) t(\omega)\, e^{-i\omega(t-(x_1-\ell)/c)}\, \mathrm{d}\omega\right], & x_1 \in (\ell, \infty), \end{cases} \tag{5.3}$$

with $\hat{s}(\omega)$ the Fourier transform of $s(t)$ (and $\Re[X]$ means real part of X). We consider incident pulses with increasing spectral contents $c\tau/h = 3, 2, 1$ (corresponding $\hat{s}(\omega)$ are shown in figure 8).

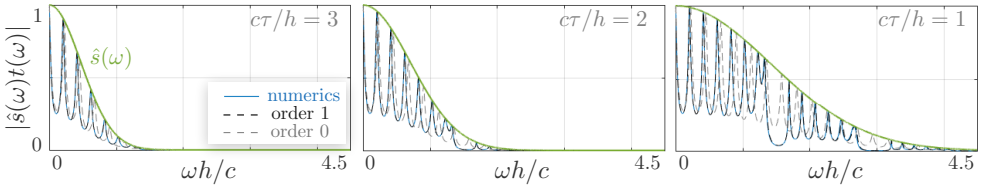

FIG. 8. *Spectral contents $\hat{s}(\omega)$ of the incident pulse and corresponding variations of $\hat{s}(\omega)t(\omega)$ contributing to the transmitted pulse, see (5.3).*

The resulting pressure profiles $p(x_1,t)$ along $x_1/h \in (-200,0) \cup (2,200)$ at dimensionless time $ct/h = 175$ are shown in figure 9. In the reported cases, we observe that the two ballistic pulses at $x_1 = \pm ct/h$, directly reflected and transmitted by the slab, are followed by pulses having undergone multiple reflections within the slab. For $c\tau/h = 3$, the most visible pulses correspond to internal reflections between the two extremities of the labyrinth, thus separated in space by $\Delta x_1 \sim 2N\ell = 28$, *i.e.*, twice the length of the entire slots. However, zooming in on a region between two of them reveals the presence of additional lower amplitude pulses due to multiple reflections/transmissions at the turning regions (hence separated in space by $\Delta x_1 \sim 2\ell = 4$). By increasing τ, the amplitudes of these pulses increase because the incident waves with shorter wavelengths are more efficiently scattered due to Bragg resonances. In terms of the accuracy of the effective models, this complexification in the scattering properties is accompanied by a neat degradation in the accuracy of the model at order 0 which ignores the Bragg scattering. As a consequence, the amplitudes of the main pulses, in addition to their positions, are not correctly predicted because the energy redistributions in reflection and transmission at the turning regions are not taken into account. In contrast the model at the order 1, by correctly taking into account the two scatterings, remains very accurate (the table 1 gives the quantitative errors $|p(x_1,t) - p_{\rm model}(x_1,t)|/|p(x_1,t)|$ in reflection and transmission for the two models).

6. Conclusions. We have provided a model capable of accurately reproducing the scattering properties of a coiled metacrystal producing high transmission due to Fabry-Pérot resonances and low transmission due to Bragg resonances in a low

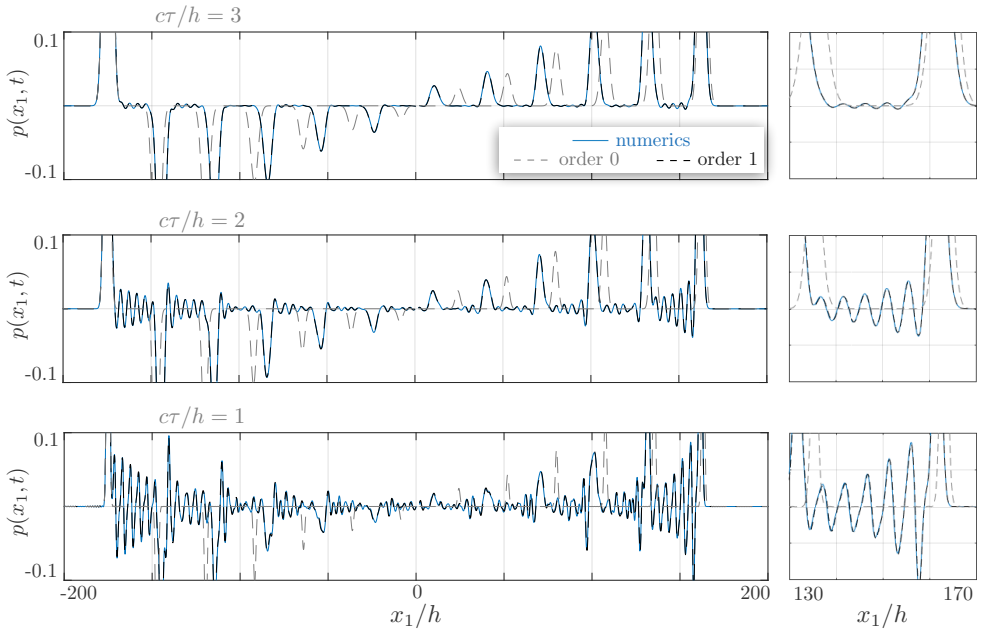

FIG. 9. *Pressure profiles along x_1 for $ct/h = 175$ for increasing spectral content of the incident pulse (for readability, the vertical range has been shortened to (-0.1,0.1), with the main pressure peaks on the order of unity).*

errors in reflection / transmission		
$c\tau/h$	model at order 0	model at order 1
3	44.6% / 77.8%	0.9% / 1.5%
2	54.4% / 95.2%	1.6% / 2.8%
1	64.3% / 123.2%	4.6% / 8.0%

TABLE 1

Errors in reflection $|p(x_1 < 0, t) - p_{model}(x_1 < 0, t)|/|p(x_1 < 0, t)|$ and in transmission $|p(x_1 > \ell, t) - p_{model}(x_1 > \ell, t)|/|p(x_1 > \ell, t)|$ for the models at the orders 0 and 1.

frequency regime (with a unique diffraction order). The effect of the Bragg resonances has been efficiently captured by taking into account the evanescent fields responsible for the scattering strength of the turning regions, these regions playing the role of atoms in a one-dimensional coiled crystal. Such metacrystalline structures offer new degree of freedom to control the acoustic flow since they allow an efficient filtering of the frequencies (perfect or negligible transmission and reflection) by simply playing on the geometry of the turning regions. We notice that additional degrees of freedom can be easily taken into account with the same formalism, such as a coiled crystal with different turning regions (different atoms) or different inter-distances between them. Another extension, although less straightforward, is to consider a more complex crystalline structure in which the turning regions become regions connecting several

slots.

Acknowledgments. J.Z.H. and K.P. are grateful for the support of the Agence de l'Innovation de Défense (AID) from the Direction Générale de l'Armement (DGA) under grant nos. 2019 65 0070 and 2019 65 0042.

REFERENCES

[1] R. Al Jahdali and Y. Wu, *High transmission acoustic focusing by impedance-matched acoustic meta-surfaces*, Applied Physics Letters, 108 (2016), p. 031902.
[2] F. Cai, F. Liu, Z. He, and Z. Liu, *High refractive-index sonic material based on periodic subwavelength structure*, Applied Physics Letters, 91 (2007), p. 203515.
[3] B. Delourme, S. Fliss, P. Joly, and E. Vasilevskaya, *Trapped modes in thin and infinite ladder like domains. part 1: Existence results*, Asymptotic Analysis, 103 (2017), pp. 103–134.
[4] B. Delourme, H. Haddar, and P. Joly, *Approximate models for wave propagation across thin periodic interfaces*, Journal de mathématiques pures et appliquées, 98 (2012), pp. 28–71.
[5] B. Delourme, E. Lunéville, J.-J. Marigo, A. Maurel, J.-F. Mercier, and K. Pham, *Approximate models for wave propagation across thin periodic interfaces*, Proceedings of the Royal Society A, 477 (2021), p. 2020.0668.
[6] P. Joly and A. Semin, *Construction and analysis of improved kirchoff conditions for acoustic wave propagation in a junction of thin slots*, ESAIM Proc., 25 (2008), pp. 44–67.
[7] Y. Li, B. Liang, Z.-m. Gu, X.-y. Zou, and J.-c. Cheng, *Unidirectional acoustic transmission through a prism with near-zero refractive index*, Applied Physics Letters, 103 (2013), p. 053505.
[8] Y. Li, B. Liang, X. Tao, X.-f. Zhu, X.-y. Zou, and J.-c. Cheng, *Acoustic focusing by coiling up space*, Applied Physics Letters, 101 (2012), p. 233508.
[9] Y. Li, B. Liang, X.-y. Zou, and J.-c. Cheng, *Extraordinary acoustic transmission through ultrathin acoustic metamaterials by coiling up space*, Applied Physics Letters, 103 (2013), p. 063509.
[10] Z. Liang, T. Feng, S. Lok, F. Liu, K. B. Ng, C. H. Chan, J. Wang, S. Han, S. Lee, and J. Li, *Space-coiling metamaterials with double negativity and conical dispersion*, Scientific reports, 3 (2013), pp. 1–6.
[11] Z. Liang and J. Li, *Extreme acoustic metamaterial by coiling up space*, Physical Review Letters, 108 (2012), p. 114301.
[12] M.-H. Lu, X.-K. Liu, L. Feng, J. Li, C.-P. Huang, Y.-F. Chen, Y.-Y. Zhu, S.-N. Zhu, and N.-B. Ming, *Extraordinary acoustic transmission through a 1d grating with very narrow apertures*, Physical Review Letters, 99 (2007), p. 174301.
[13] J.-J. Marigo and A. Maurel, *Homogenization models for thin rigid structured surfaces and films*, The Journal of the acoustical Society of America, 140 (2016), pp. 260–273.
[14] J.-J. Marigo and A. Maurel, *Second order homogenization of subwavelength stratified media including finite size effect*, SIAM Journal on Applied Mathematics, 77 (2017), pp. 721–743.
[15] P. Martin and A. Skvortsov, *On blockage coefficients: flow past a body in a pipe*, Proceedings of the Royal Society A, 478 (2022), p. 20210677.
[16] M. Molerón, M. Serra-Garcia, and C. Daraio, *Acoustic fresnel lenses with extraordinary transmission*, Applied Physics Letters, 105 (2014), p. 114109.
[17] S. Qi, Y. Li, and B. Assouar, *Acoustic focusing and energy confinement based on multilateral metasurfaces*, Physical Review Applied, 7 (2017), p. 054006.
[18] E. Tuck, *Some classical water-wave problems in varying depth*, in Waves on Water of Variable Depth, Springer, 2005, pp. 9–20.
[19] Y. Xie, B.-I. Popa, L. Zigoneanu, and S. A. Cummer, *Measurement of a broadband negative index with space-coiling acoustic metamaterials*, Physical Review Letters, 110 (2013), p. 175501.
[20] N. Yu and F. Capasso, *Flat optics with designer metasurfaces*, Nature materials, 13 (2014), pp. 139–150.
[21] J. Zhou Hagström, A. Maurel, and K. Pham, *Revisiting effective acoustic propagation in labyrinthine metasurfaces*, Submitted, (2022).